Hierarchical Nanostructures of Nitrogen-Doped Porous Carbon Polyhedrons Confined in Carbon Nanosheets for High-Performance Supercapacitors

Zhe Zhao,[†] Siliang Liu,[†] Jixin Zhu,[‡] Jingsan Xu,[§] Le Li,[†] Zhaoqi Huang,[†] Chao Zhang,*,[†] and Tianxi Liu*,[†]

[†] State Key Laboratory for Modification of Chemical Fibers and Polymer Materials, College of Materials Science and Engineering, Innovation Center for Textile Science and Technology, Donghua University, Shanghai 201620, P. R. China

[‡] Key Laboratory of Flexible Electronics (KLOFE) & Institute of Advanced Materials (IAM), Jiangsu National Synergetic Innovation Center for Advanced Materials (SICAM), Nanjing Tech University (Nanjing Tech), 30 South Puzu Road, Nanjing 211816, China

[§] School of Chemistry, Physics and Mechanical Engineering, Queensland University of Technology, Brisbane, Queensland 4001, Australia

Ⓢ *Supporting Information*

ABSTRACT: Interconnected close-packed nitrogen-doped porous carbon polyhedrons (NCPs) confined in two-dimensional carbon nanosheets (CNSs) have been prepared through a sustainable one-pot pyrolysis of a simple solid mixture of zeolitic imidazolate framework-8 (ZIF-8) crystals and with organic potassium as the precursors. The hierarchically organized framework of the NCP−CNS composites enables NCPs and CNSs to act as well-defined electrolyte reservoirs and mechanical buffers accommodating large volume expansions of NCPs, respectively. Among the unique composite nanostructures, the NCPs with vast micropores provide electric double-layer capacitances, while the CNSs bridge the individual NCPs to form a conductive pathway with a hierarchical porosity. As a result, the NCP−CNS composites with high electrical integrity and structural stability are used as electrode materials for high-performance supercapacitors, which exhibit excellent electrochemical capacitive characteristics in terms of an outstanding capacitance of 300 F g^{-1} at 1 A g^{-1}, large energy density of 20.9 W h kg^{-1}, and great cycling performance of 100% retention after 6000 cycles. This work therefore presents a one-pot and efficient strategy to prepare an ordered arrangement of ZIF-8-derived porous carbons toward new electrode materials in promising energy storage systems.

KEYWORDS: ZIF-8, N-doped porous carbon polyhedrons, carbon nanosheets, hierarchical nanostructure, supercapacitors

ZIF-8

+

potassium citrate

800 °C, N$_2$

NCP-CNS composites
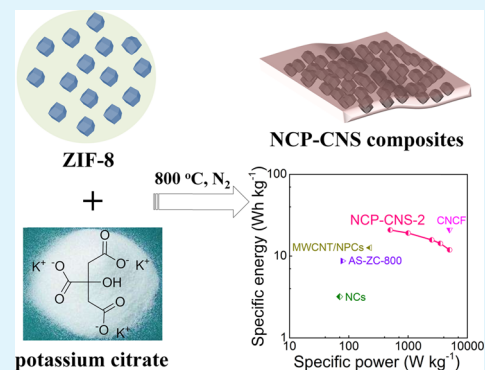
1. INTRODUCTION

There is always an urgent demand for developing low-cost and environmental-friendly energy storage systems with the sustainable development of economy and society in recent years. Supercapacitors have received abundant attentions because of their high power density, fast charge/discharge rate, and good cycling performance.[1−3] Supercapacitors are typically classified into electric double-layer capacitors (EDLCs) and pseudocapacitors.[4−6] Although the pseudocapacitors could deliver attractive values of energy density,[7] several tough problems of the pseudocapacitive materials such as high cost and unsatisfying cycling/rate performances are urgently to be addressed before considering their actual applications.[6,8−10] On the contrary, although the energy density of EDLCs is relatively lower than that of pseudocapacitors, the extremely stable cycling stability and excellent rate performance of the EDLCs find new ways for practical energy storage applications especially in high-power energy storages. Carbon materials are widely employed as electrode materials for EDLCs owing to their long cycling stability, abundant porosity, excellent electrical conductivity, and chemical stability.[11,12] Generally, the capacitance of these carbon materials is closely connected with their specific surface area and pore structures.[13] Therefore, various methods have been adapted to enhance the surface area of porous carbon materials applied to promising electrode materials for EDLCs.

Metal−organic frameworks (MOFs) are three-dimensional (3D) long-range ordering assemblies of transition-metal clusters and corresponding organic frameworks.[14−16] Among MOFs, zeolitic imidazolate framework-8 (ZIF-8) is an important subclass of MOFs, which consists of Zn ions and imidazole frameworks.[17,18] Large pore volume, high carbon/

nitrogen contents, and good thermal stability of ZIF-8 make it an ideal precursor for the synthesis of porous carbons with extremely high surface area and large pore volume via a simple and straightforward pyrolysis.[19−22] It should be specially noted that porous carbons with a rich nitrogen doping could provide considerable pseudocapacitances, which therefore play important roles in big improvements of the electrochemical performances.[23−25] Nitrogen-doped porous carbons derived from ZIF-8 usually process abundant nitrogen content, large specific surface area, and preserved porosity, which synergistically enhance the resultant electrochemical performances.[26−28] However, the directly pyrolyzed ZIF-8, often denoted as N-doped porous carbon polyhedrons (NCPs), typically shows unsatisfying electrochemical capacitive performances for EDLCs.[29] It is anticipated that the specific capacitance value of the resultant porous carbon materials increases with the increase of the surface area. Micropores with an average pore size smaller than 1 nm could enhance the specific capacitance of electrode materials.[30] However, the micropores in NCPs (pore sizes of ∼1.5 nm) have a detrimental effect on the resultant capacitances. In addition, when evaluated as an electrode material, it is extremely hard to construct interconnected conductive networks for fast charge transfers using only individual particles of NCPs. Therefore, it is necessary to construct the structural design of NCPs with a hierarchical porosity, which can greatly boost the energy density of NCP electrodes by the integration of desirable features such as large surface area, large nitrogen content, and high electrochemical stability.[31−34]

Herein, we present a straightforward synthesis of hierarchical nanostructures by confining close-packed NCPs into two-dimensional (2D) carbon nanosheets (CNSs). The whole preparation is extremely simple through a one-pot pyrolysis of a solid mixture of ZIF-8 crystals and potassium citrate at high temperatures. During the pyrolysis, potassium citrate was used as carbon sources transferring into CNSs, and ZIF-8 crystals were used as both carbon and nitrogen precursors to create the NCPs with abundant micropores. In the resultant nanostructures, individual NCP particles confined in the 2D CNS frameworks could connect with each other to form a multidimensional conductive network. The CNSs could effectively buffer inevitable volume changes of NCPs especially during the charge/discharge cycles. Because of the presence of abundant micropores within the embedded NCPs, the NCP−CNS composites provide a hierarchical porosity with further packed CNSs, which is extremely favorable for efficient ion transfers. Meanwhile, the nitrogen doping among the NCP−CNS composites also achieves an enhanced electrochemical performance. As a result, the resultant NCP−CNS composites show excellent electrochemical performances, revealing high specific capacitance, long cycling life, and outstanding energy density.

2. EXPERIMENTAL SECTION

2.1. Materials. Zinc nitrate hexahydrate ($Zn(NO_3)_2 \cdot 6H_2O$), zinc acetate ($Zn(CH_3COO)_2$), 2-methylimidazole (MIM), potassium citrate, and hydrochloric acid (HCl, 37%) were purchased from Sinopharm Chemicals. All the reagents were used as received without further purification.

2.2. Synthesis of the s-ZIF-8. $Zn(NO_3)_2 \cdot 6H_2O$ (0.4 g) and MIM (0.88 g) were mixed together and ground using a motor for 5 min. Methanol (38.5 mL) was then added to form a solution, which was aged for 1 h at room temperature to form a milky colloidal solution.

The product was centrifuged, washed with methanol at least three times, and dried at 60 °C for 12 h in vacuum.

2.3. Synthesis of the m-ZIF-8. $Zn(CH_3COO)_2$ (0.4 g) and MIM (0.6 g) were mixed together and ground using a motor for 5 min. Methanol (100 mL) was then added to form a solution, which was aged for 24 h at room temperature. The product was centrifuged, washed with methanol at least three times, and dried at 60 °C for 12 h in vacuum.

2.4. Synthesis of the l-ZIF-8. $Zn(CH_3COO)_2$ (0.4 g) and MIM (0.6 g) was dissolved in 50 mL of methanol. The two solutions were mixed and stirred for 5 min. The solution was aged for 24 h at room temperature. The product was centrifuged, washed with fresh methanol at least three times, and dried at 60 °C for 12 h in vacuum.

2.5. Synthesis of the NCPs. The ZIF-8 was used as the carbon and nitrogen precursors to obtain the NCPs with different particle sizes. The ZIF-8 powder was heated at 800 °C at a heating rate of 5 °C min^{-1} in a nitrogen atmosphere. After cooling, the products were washed with 0.5 M HCl solution to remove residual zinc components and dried at 60 °C for 12 h in vacuum. The NCPs prepared from s-ZIF-8, m-ZIF-8, and l-ZIF-8 were called s-NCP, m-NCP, and l-NCP, respectively.

2.6. Synthesis of the NCP−CNS Composites. The s-ZIF-8 powder (0.3 g) was ground with a certain amount of potassium citrate for 10 min. The mixed powder was then heated at 800 °C at a heating rate of 5 °C min^{-1} for 2 h. The products were washed with 0.5 M HCl solution and dried at 60 °C for 12 h in vacuum. The weight ratios of s-ZIF-8 and potassium citrate were tuned at 1/5, 1/15, and 1/45, thus giving the products denoted as NCP−CNS-1, NCP−CNS-2, and NCP−CNS-3, respectively. For comparison, potassium citrate was directly carbonized according to the same procedure, giving the product denoted as CNSs.

2.7. Characterizations and Electrochemical Measurements. See details in the Supporting Information.

3. RESULTS AND DISCUSSION

The preparation of the NCP−CNS composites is depicted in Figure 1. The ZIF-8 crystals and potassium citrate were ground
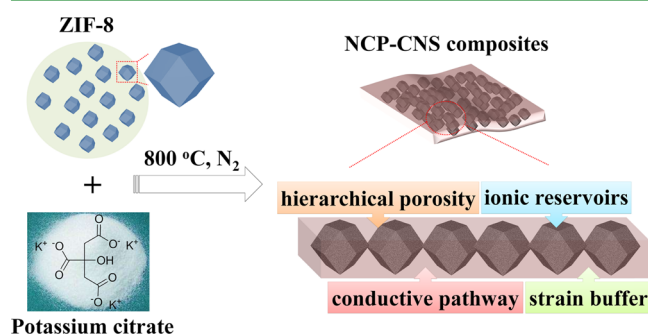
Figure 1. Schematic illustration of the formation of the NCP−CNS composites.

to form a powder mixture, which was then pyrolyzed at the temperature of 800 °C for 2 h under a nitrogen flow, washed with 5% HCl, and then dried in vacuum at 60 °C. The carbonization yields of ZIF-8 crystals and potassium citrate at the temperature of 800 °C are 40 and 5%, respectively, which are quite different from each other. Therefore, the resultant NCP−CNS composites were denoted as NCP−CNS-1, NCP−CNS-2, and NCP−CNS-3, indicating the ZIF-8/potassium citrate mass ratios of 1:5, 1:15, and 1:45, respectively. The NCP−CNS composites with the ZIF-8/potassium citrate mass ratios of 1:25 and 1:35 were also prepared under the same pyrolysis condition, which are denoted as NCP−CNS-4 and NCP−CNS-5. Ideally, the weight percentages of NCPs within

the NCP−CNS-1, NCP−CNS-2, NCP−CNS-4, NCP−CNS-5, and NCP−CNS-3 are about 61.5, 34.8, 24.2, 18.6, and 15.1%, respectively. Therefore, for clarity, NCP−CNS-1, NCP−CNS-2, and NCP−CNS-3 were chosen for detailed investigations because of their appropriate gradient contents of NCPs among the NCP−CNS composites. With an optimized ratio of ZIF-8 and potassium citrate, the resultant NCP−CNS composites are expected to exhibit hierarchical porosities with efficient ionic reservoirs because of embedded NCPs with large micropores. In addition, the surrounded CNSs could act as mechanical buffers accommodating the volume expansion of embedded NCPs and inhibiting the aggregation of NCPs, thus maintaining high electrical integrity and structural stability of the NCP−CNS composites as electrode materials for supercapacitors. For comparison, neat NCPs and CNSs were also prepared using only ZIF-8 and potassium citrate, respectively.

The particle sizes of ZIF-8 crystals as well as the resultant NCPs can be precisely controlled by changing different synthetic methods,[35] and for clarity, three batches of ZIF-8 crystals were prepared for the investigation of the assembly behavior and electrochemical performances of NCPs in a variety of particle sizes. The as-obtained ZIF-8 with a mean diameter of 90, 600, and 1900 nm was denoted as s-ZIF-8, m-ZIF-8, and l-ZIF-8, respectively, confirmed by scanning electron microscopy (SEM) in Figure S1. X-ray diffraction (XRD) and Raman spectra were measured to identify the crystal structures and compositions of the ZIF-8 with different particle diameters. All the XRD patterns of s-ZIF-8, m-ZIF-8, and l-ZIF-8 are in good agreement with the standard diffractions of ZIF-8 (Figure S2a).[36−38] The formation of s-ZIF-8, m-ZIF-8, and l-ZIF-8 can be further confirmed by the Raman spectra (Figure S2b), which show bands perfectly corresponding to the MIM linker.[39]

The ZIF-8 crystals could turn into NCPs through a simple pyrolysis, and the resultant NCPs were denoted as s-NCPs, m-NCPs, and l-NCPs, using the precursor of s-ZIF-8, m-ZIF-8, and l-ZIF-8, respectively. The average particle sizes of s-NCPs, m-NCPs, and l-NCPs were calculated as 60, 350, and 1700 nm, respectively (Figure S3). The shapes of all the NCPs remain well after the pyrolysis, and slight decreases in size and crumpled surfaces are observed. During pyrolysis, Zn ions were reduced to Zn at high temperature, which were finally removed by acid washing. The diffraction pattern at $2\theta = 25°$ belongs to the (002) crystal plane of graphitic structures (Figure S4a), indicating a high graphitization degree of NCPs.[40] In addition, no other diffraction patterns could be observed, indicating that all the ZIF-8 was converted into carbon materials during the pyrolysis. The Raman spectra of s-NCPs, m-NCPs, and l-NCPs are measured and illustrated in Figure S4b. The G band at ~1580 cm^{-1} demonstrates the existence of the graphitic carbon while the typical D band at ~1345 cm^{-1} implies the defects and heteroatoms of graphitic lattices.[40] The intensity ratios of G band to D band are constant (~1), indicating the intrinsic graphitic features of the NCPs. The nitrogen adsorption/desorption isotherms of s-NCPs, m-NCPs, and l-NCPs are shown in Figure S5. All the isotherms belong to type I isotherms, indicating typical micropore structures among these NCPs. The specific area of NCPs declines compared with the precursor ZIF-8 because of the collapsing of pore channels, as summarized in Table S1. Taking the s-NCPs as an example, the specific surface area of s-NCPs reduces to 824 m^2 g^{-1} whereas the specific surface area of s-ZIF-8 is 1253 m^2 g^{-1}. Upon pyrolysis, at the high relative pressure of 0.8 to 1.0, the s-NCPs give the adsorption isotherm with a step confirming the

unconsolidated porous structures because of particle packing of s-NCPs.

The effects of NCP particle sizes on the resultant electrochemical behaviors were then systemically investigated. The electrochemical properties of s-NCPs, m-NCPs, and l-NCPs were evaluated by cycle voltammetry (CV) and galvanostatic charge/discharge measurements assembled in a symmetric supercapacitor with 6 M KOH as electrolytes. At the scan rate of 10 mV s^{-1}, the rectangular shapes of the CV curves of NCPs indicate a typical electric double-layer capacitive behavior (Figure S6a).[41] The CV curves of s-NCPs exhibit larger surrounded area than those of m-NCPs and l-NCPs, indicating that the s-NCPs have the highest specific capacitance among all the NCPs with different sizes. The galvanostatic charge/discharge curves were measured at different current densities to precisely calculate the specific capacitances of the NCPs (Figure S6b,c). All electrodes display a triangle shape in the potential range from 0 to 1 V. Among all the NCPs, the iR drops which are smaller than 0.1 V at 1 mA g^{-1} could be observed in the discharge curves, implying the tiny resistances of ion transport with the electrodes. Specifically, the s-NCPs show the specific capacitance value of 170 F g^{-1}, which is higher than those of m-NCPs (148 F g^{-1}) and l-NCPs (128 F g^{-1}). The results could be explained that in the s-NCPs, the decreased size of s-NCPs may enhance a facile penetration of electrolytic ions into the deep pores.[41,42] Figure S6d presents the electrochemical impedance spectroscopy (EIS) curves of s-NCPs, m-NCPs, and l-NCPs, and the larger slope of s-NCPs clearly indicates a better capacitive behavior of s-NCPs compared with m-NCPs and l-NCPs. Given that, s-ZIF-8 was chosen as the precursor for the preparation of the NCP−CNS composites. For clarity, the NCPs appearing on their own refer to s-NCPs in the following.

The morphology of the NCP−CNS composites was further measured by SEM observations. The synthesized NCPs exhibit a regular shape of dodecahedra with an average particle size of ~60 nm (Figure 2a,b). Layered and crumpled structures with randomly opened macrospores are found within the NCP−CNS composites, where the CNSs are with a lateral size of micrometer scale and the NCPs are embedded in the interconnected CNS frameworks (Figure 2c−h). The CNSs exhibit an interconnected structure, which could provide a multidimensional pathway for an electron transfer (Figure 2i,j). A porous and wrinkled surface can be observed from high-magnification SEM images for the NCP−CNS composites (Figure 2i,l). Internal morphologies of the NCP−CNS-2 can be observed using the ground samples (Figure S7). The NCP particles embedded in the CNSs can be clearly observed especially in the high-magnification SEM images. Transmission electron microscopy (TEM) images of the NCP−CNS composites also provide closer observations of the embedded composite structures (Figure 3). Individual NCPs are uniformly dispersed in the 2D frameworks formed by the CNSs. No aggregation of NCPs could be observed because of the unique confinement of CNSs and, in other words, the NCP "islands" are bridged with the continuous CNSs. The NCPs are assembled and imbedded into 2D CNS networks, thus forming a multidimensional functional material. Combined with large micropore volume within the NCPs, the unique structures of the NCP−CNS composites provide a hierarchical porosity as well as fast electron transport.

The growth mechanism of the NCP−CNS composites with hierarchical nanostructures of NCPs embedded in CNSs was
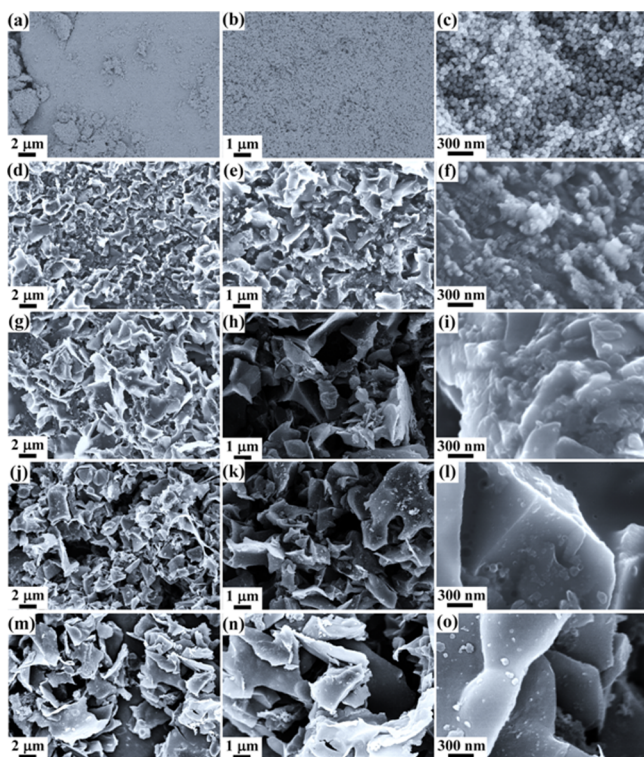
Figure 2. SEM images of (a−c) NCPs, (d−f) NCP−CNS-1, (g−i) NCP−CNS-2, (j−l) NCP−CNS-3, and (m−o) CNSs at low and high magnifications, respectively.
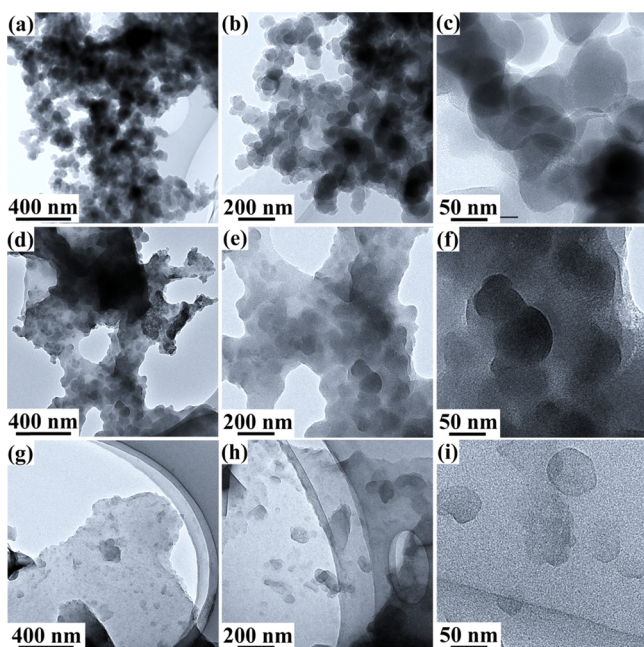

Figure 3. TEM images of (a−c) NCP−CNS-1, (d−f) NCP−CNS-2, and (g−i) NCP−CNS-3 at different magnifications, respectively.

intensively investigated. The contrast experiments of pyrolysis of citric acid and simple mixture of ZIF-8 and citric acid (mass ratio of 1:15) were conducted to investigate the formation mechanism of the final nanostructure. SEM images of the directly pyrolyzed samples using citric acid and a simple mixture of ZIF-8 and citric acid as the precursor, respectively, were measured and are shown in Figure S8. Figure S8a−c

indicates the pyrolyzed sample of neat citric acid that shows irregular-shaped particles with sizes up to hundreds of micrometers, and the thickness of the sample is much larger than those of CNSs (Figure 2m−o). The pyrolyzed sample of the simple mixture of ZIF-8 and citric acid (Figure S8d−f) shows a similar irregular morphology as the pyrolyzed sample of citric acid. Compared with NCP−CNS-2, the pyrolyzed sample of the mixture of ZIF-8 and citric acid forms a more flat and enormous cross-sectional surface, and the morphology of the composites shows that the NCPs are embedded in the large carbon bulks. Close observations from the cross-sectional surface of the pyrolyzed sample of mixture of ZIF-8 and citric acid show that the NCPs are uniformly embedded within the matrix. Therefore, heterogeneous nucleation carbonization processes are utilized to make clear the growth mechanism of NCPs confined in CNSs during the pyrolysis of ZIF-8 and potassium citrate. In case of the primary stage of pyrolysis, the decomposition and carbonization of potassium citrate could take place especially on the surface of ZIF-8 particles because of good chemical stability of the ZIF-8. With the progress of further carbonization process, the intermediate product derived from potassium citrate on individual ZIF-8 particles may contact together for further couplings and, importantly, the presence of potassium ions could play key roles in stabilizing the 2D structure of CNSs by preventing their further stacking into irregular particles.[43−45]

Figure 4a shows XRD patterns of the NCP−CNS composites. All the samples display two obvious diffraction patterns at $2\theta = 25°$ and $45°$, revealing the successful pyrolysis from precursors of ZIF-8 and organic salts into carbon materials.[40,46] Raman spectra were measured to further investigate the carbon structures and are illustrated in Figure 4b. All the samples exhibit two typical bands at 1340 and 1590 cm^{-1}, respectively, which is ascribed to D and G bands, respectively. The D band represents the defects and disorders of carbon structures, while the G band describes the sp^2 type carbon among the materials.[47−49] The intensity ratio of D/G increases from 0.96 to 0.99 with the increasing contents of CNSs within the NCP−CNS composites, indicating that the introduction of CNSs into the NCP−CNS composites promotes fewer graphitic crystallites with more defects. The pore structures of the prepared samples were further confirmed by the nitrogen adsorption/desorption measurements. Figure 4c,d exhibits the nitrogen adsorption/desorption isotherms as well as the pore size distributions of the NCP−CNS composites compared with neat NCPs and CNSs (summarized in Table 1). NCP samples exhibit typical type I isotherms; however, all the other samples exhibit both type I isotherms of micropores and type IV isotherms of mesopores because of the packaging of NCPs between the CNS layer.[50,51] The BET surface area of the CNS sample is 582 m^2 g^{-1}, whereas the nitrogen adsorption of the NCPs shows a typical type-I adsorption with specific surface area of 825 m^2 g^{-1} comparable with the reported values.[41,52] The surface areas of the NCP−CNS composites first increase to 1285 m^2 g^{-1} of the NCP−CNS-1, 1727 m^2 g^{-1} of the NCP−CNS-2, relative to NCPs with increasing the CNS content, and then decrease to 1067 m^2 g^{-1} of the NCP−CNS-3. Mesopores with an average size above 2 nm are found in all the composites, which can be attributed to the unique architectures derived from the CNS-bridged NCPs. Open pores can be concluded in all the composites through the pore size distribution curves, which are consistent with SEM and TEM observations. For comparisons, the BET surface area
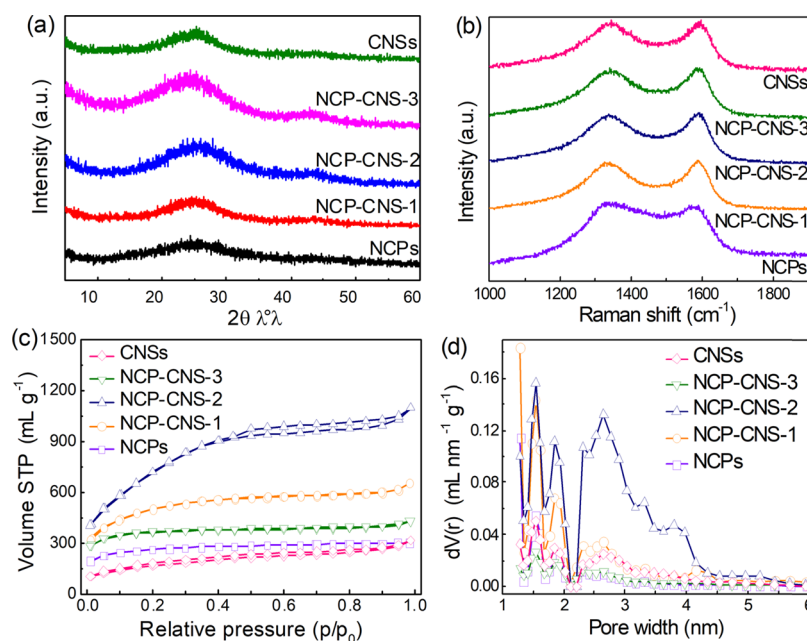
Figure 4. (a) XRD patterns, (b) Raman spectra, (c) nitrogen adsorption/desorption isotherms, and (d) pore size distributions of the NCP−CNS composites compared with neat NCPs and CNSs.

Table 1. BET Surface Areas and Pore Size Distributions of the NCP−CNS Composites, NCPs, and CNSs

sample	S_{BET} [m^2 g^{-1}]	total pore volume [mL g^{-1}]	micropore volume [mL g^{-1}]	mesopore volume [mL g^{-1}]
NCPs	825	0.42	0.34	0.08
NCP−CNS-1	1285	0.86	0.60	0.26
NCP−CNS-2	1727	1.48	0.69	0.79
NCP−CNS-3	1067	0.57	0.50	0.07
CNSs	582	0.41	0.19	0.22

and pore volume data of the NCP−CNS-2 samples prepared at different heating temperatures of 2.5, 5, and 10 °C min^{-1} are measured and summarized in Table S2. The NCP−CNS-2 at the heating rate of 5 °C min^{-1} exhibits the highest specific surface area, which is higher than those of the composites at the heating rate of 2.5 °C min^{-1} (1266 m^2 g^{-1}) and 10 °C min^{-1} (1001 m^2 g^{-1}). The interconnected mesopores favor the high-rate electron transfer pathway,[53,54] whereas the vast micropores play key roles in acting as ion reservoirs for enlarging the electric double-layer surfaces and thus enhancing the specific capacitances.

The elemental compositions of carbon, hydrogen, nitrogen, and oxygen within the NCPs, NCP−CNS composites, and CNSs were investigated and are shown in Figure S9. The high mass ratio of nitrogen can be observed in the NCPs and NCP−CNS-2 samples, indicating the presence of efficient nitrogen doping within the NCPs and NCP−CNS-2, which could provide pseudocapacitive performance to further improve the specific capacitance value of the NCP−CNS composite electrodes. The C/O weight ratios of NCPs, NCP−CNS-2, and CNSs were calculated to be 16.2, 11.6, and 8.2, respectively. The NCP−CNS-2 exhibits a relatively high content of oxygen, indicating the oxygen-containing groups within the NCP−CNS composites might create additional pseudocapacitive performance to further improve the specific capacitance of the composite materials. High-resolution N 1s X-ray photoelectron spectroscopy (XPS) survey spectra of the

NCP−CNS composites, NCPs, and CNSs were measured and are shown in Figure S10. The peaks at 400.8, 400, and 398.3 eV are attributed to graphitic nitrogen, pyrrolic nitrogen, and pyridinic nitrogen, respectively, among the nitrogen-doped carbon of the NCP−CNS composites as well as the NCPs. No peak ascribing to the nitrogen can be observed in the neat CNS sample, indicating the successful nitrogen doping of CNSs because of the presence of nitrogen sources within the ZIF-8. The electrical conductivities of the NCP−CNS composites compared with neat NCPs and CNSs were investigated by a four-probe measurement, and the electrical conductivity values of all the samples are summarized in Table S3. Because of the unique structures of NCPs confined in 2D CNSs, the NCP−CNS-2 exhibits a superior electrical conductivity of 1.4 S m^{-1}, compared with that of neat CNSs (0.72 S m^{-1}), implying a fast ion transport among the NCP−CNS composites.

Figure 5a exhibits the typical CV curves of the NCP−CNS composites compared with neat NCPs and CNSs. The CV curves of all the samples display nearly rectangular shapes, which implies that the electrochemical capacitive behaviors of the obtained samples are ideal electric double-layer capacitance. The CV curves of the NCP−CNS composites exhibit a larger area compared with neat NCPs and CNSs, and the NCP−CNS-2 sample shows the largest area, indicating the highest specific capacitance value of the NCP−CNS-2 electrode compared with the others. The CV curves of the NCP−CNS-2 electrode at different scan rates were measured and are shown in Figure 5b. With the increased scan rates, the areas of the CV curves are gradually increasing and, most importantly, when the scan rate increases up to 100 mV s^{-1}, the CV curves of the NCP−CNS-2 electrode still remain in good rectangular shape with little distortions, indicating a great rate capability, especially at high scan rates, because of remarkable ion propagations within the electrode matrix. The superior electrochemical performances of the NCP−CNS composites were further investigated by the galvanostatic charge/discharge measurements. Figure S11a exhibits the galvanostatic charge/discharge curves of the NCP−CNS composites, neat CNSs and
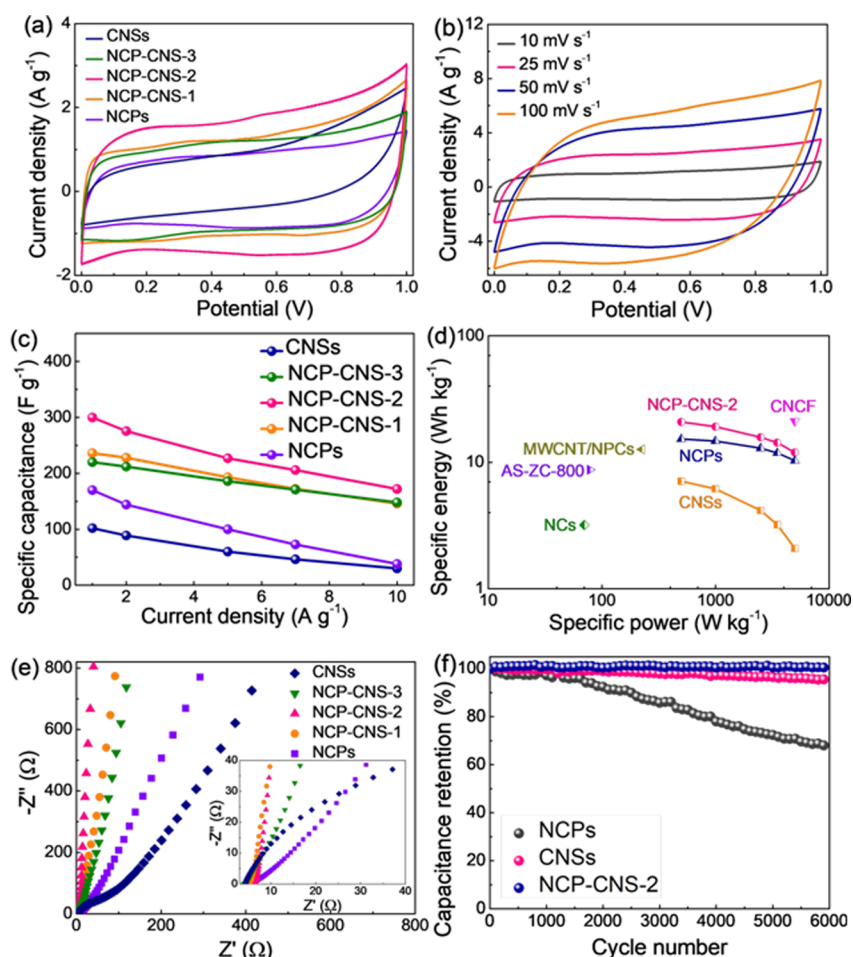
Figure 5. (a) CV curves of the NCP−CNS composites compared with NCPs and CNSs at 10 mV s^{-1}. (b) CV curves of the NCP−CNS-2 electrode at different scan rates. (c) Specific capacitances of NCP−CNS composites compared with NCPs and CNSs calculated from the galvanostatic charge/discharge curves at different current densities. (d) Ragone plots for comparison of our supercapacitors with various ZIF-8-derived carbons and their composite materials previously reported. (e) EIS curves of NCP−CNS composites compared with NCPs and CNSs. (f) Cycling stability of NCP−CNS-2, NCPs, and CNSs.

NCPs at 1 A g^{-1} within a potential range from 0 to 1 V, and all the curves show typical linear charge/discharge curves. The NCP−CNS composite electrodes exhibit relatively low iR drops in the discharge curves compared with those of neat NCPs and CNSs, indicating their relatively low internal resistances. The galvanostatic charge/discharge curves of the NCP−CNS-2 electrode at different current densities are shown in Figure S11b, which imply well-balanced charge storages and the ability of such electrodes to deliver high power. The comparisons of the specific capacitances with different current densities of various samples were calculated and are displayed in Figure 5c. The NCP−CNS composites exhibit much larger specific capacitance values than those of NCPs and CNSs. Specifically, the NCP−CNS-2 shows a superior capacitive performance holding a specific capacitance of 300 F g^{-1} at 1 A g^{-1}, which is much higher than those of NCPs (170 F g^{-1}) and CNSs (102 F g^{-1}). Meanwhile, the NCP−CNS-2 electrode achieves the capacitance retention of 57% when the current density increases from 1 to 10 A g^{-1}, which is much higher than those of NCPs (22%) and CNSs (29%), indicating its superior rate capacitances because of favorable and rapid electron/ion transfer. Taking the NCP−CNS composites into consideration, the NCP−CNS-2 electrode exhibits the best capacitive performance even at the high current density of 10 A g^{-1},

compared with those of NCP−CNS-1 (146 F g^{-1}) and NCP−CNS-3 (148 F g^{-1}). Furthermore, the specific capacitances of the NCP−CNT composites at different initial ratios of ZIF-8 and potassium citrate are calculated and compared in Figure S12. Specifically, the NCP−CNS-2 shows the highest capacitance, higher than those of other NCP−CNS composites with different initial ratios of ZIF-8 and potassium citrate.

The electrochemical parameters such as the specific capacitance values, the configurations for the assembled supercapacitor devices, as well as the electrolytes used for the NCP−CNS-2 electrodes are summarized and compared with other ZIF-8-derived electrodes for supercapacitors (Table 2). Considering the two-electrode configuration devices for the measurements and easy synthesis for the NCP−CNS composites, this study therefore provides a simple yet efficient way for the development of new electrode materials for promising energy storage. Importantly, the CV curves of the NCP−CNS-2 electrode on the graphite paper compared with neat graphite paper indicate that neat graphite paper only provides a negligible contribution to the final capacitance value of the resultant electrodes (Figure S13).

Figure 5d shows the Ragone curves to give a figurative comparison of the energy density and powder density of the supercapacitor device using our NCP−CNS composites as

Table 2. Summary of Electrochemical Parameters of NCP−CNS-2 with ZIF-8-Derived Carbons and Their Composites in the Literature

electrode materials	specific capacitance [F g^{-1}]	device configuration	electrolyte	refs
NCs	23 at 0.1 A g^{-1}	two-electrode	basic	60
CNCF	340 at 2 A g^{-1}	three-electrode	basic	61
MWCNT/NPCs	112 at 0.5 A g^{-1}	two-electrode	acidic	62
CNT@CZIF-2	324 at 0.5 A g^{-1}	three-electrode	basic	63
S-900	56.6 at 0.1 A g^{-1}	two-electrode	acidic	52
PC1000@C	225 at 0.5 A g^{-1}	three-electrode	basic	64
NPC	19 at 2.5 A g^{-1}	two-electrode	organic	65
porous N-doped carbon/CNTs	250 at 1 A g^{-1}	three-electrode	neutral	66
carbon-ZS	285.8 at 0.1 A g^{-1}	three-electrode	basic	67
MoS$_2$@MPC	189 at 1 A g^{-1}	three-electrode	acidic	68
ZIF-8 (N$_2$, 723 K)	185 at 5 mV s^{-1}	three-electrode	basic	69
LC-ZIF-8	181 at 5 mV s^{-1}	three-electrode	basic	70
Z-900	214 at 5 mV s^{-1}	three-electrode	acidic	71
AS-ZC-800	251 at 0.25 A g^{-1}	two-electrode	acidic	72
NCP−CNS-2	**300 at 1 A g^{-1}**	two-electrode	basic	**this work**

electrode materials with various ZIF-8-derived carbons and their composites previously reported.[53,55−57] Supercapacitorsusing symmetric NCP−CNS-2 electrodes show a remarkable high energy density of 20.9 W h kg^{-1} at a power density of 500 W kg^{-1}, which are calculated from the formulas illustrated in the Supporting Information.[58,59] When increasing the power density to 5000 W kg^{-1}, the energy density of our devices still maintain an energy density as high as 12 W h kg^{-1}. In addition, we have also compared the NCP−CNS-2 electrode with various ZIF-8-derived carbons and their composites previously reported in terms of specific capacitances, device configurations, and electrolytes. Taking all the samples into consideration, our NCP−CNS-2 electrode shows superior capacitive performances compared with other electrodes based on ZIF-8-derived carbons.

The EIS curves were measured and compared to further investigate the outstanding electrochemical performance of the NCP−CNS-2 electrode. Figure 5e displays the Nyquist plots of the NCP−CNS composites compared with NCPs and CNSs. The Nyquist plots of all the samples show linear traits at their low-frequency regions, and no obvious semicircles can be observed at high-frequency regions, indicating the purely capacitive behaviors and low charge-transfer resistances among these electrodes. Furthermore, compared with NCPs and CNSs, all of the line slopes of the NCP−CNS composites are very precipitous, implying the fast ion diffusion within the electrodes. Therefore, the EIS results demonstrate the synergistic effect when combining NCPs and CNSs into the composites as a promising electrode material for supercapacitors. The cycling performance of the NCP−CNS composite electrodes for supercapacitors was also evaluated by repeated galvanostatic charge/discharge tests. At 1 A g^{-1}, no capacitance loss can be observed after 6000 charge/discharge

cycles, which further demonstrates the unique advantages of the NCP−CNS composites for supercapacitor applications (Figure 5f). The NCP−CNS-2 electrode shows an extremely long cycle life of up to 6000 cycles with no capacitance loss; however, neat NCPs and CNSs exhibit a capacitance loss of 32 and 5%, respectively. The good cycling stability for the NCP−CNS-2 highlights the advantages that the NCP−CNS composites can meet the practical requirements for supercapacitor electrodes.

4. CONCLUSION

In summary, the NCP−CNS composites have been designed and prepared by a direct pyrolysis of a simple mixture of ZIF-8 and potassium citrate. The NCP−CNS composites show a unique hierarchical structure, where the NCPs are strongly wrapped and assembled within the 2D CNSs to form 3D interconnected frameworks. As a result, the NCP−CNS composites exhibit a high surface area of 1726 m^2 g^{-1}, superior specific capacitance of 300 F g^{-1}, excellent energy density of 20.9 W h kg^{-1}, and outstanding cycling life with almost no capacitance loss after 6000 cycles. This study therefore suggests a strategy for the synthesis and assembly of novel multifunctional composites of MOF-derived carbon with other carbon components, with potentials for structural evolution as well as functional applications in the near future.

■ ASSOCIATED CONTENT

Ⓢ Supporting Information

The Supporting Information is available free of charge on the ACS Publications website at DOI: 10.1021/acsami.8b03431.

> SEM images, XRD patterns, and Raman spectra of s-ZIFs, m-ZIFs, l-ZIFs, s-NCPs, m-NCPs, and l-NCPs; nitrogen adsorption/desorption isotherms and pore size distributions of s-NCPs, m-NCPs, and l-NCPs; CV curves of s-NCPs, m-NCPs, and l-NCPs; galvanostatic charge/discharge curves of s-NCPs, m-NCPs, and l-NCPs; specific capacitances of s-NCPs, m-NCPs, and l-NCPs; EIS curves of s-NCPs, m-NCPs and l-NCPs; SEM images of the NCP−CNS-2 after grinding; SEM images of pyrolysis samples of citric acid and mixture of ZIF-8 and citric acid; galvanostatic charge/discharge curves of the NCP−CNS composites; specific capacitances of the NCP−CNS composites; elemental compositions of NCP−CNS-2, NCPs, and CNSs; N 1s XPS spectra of the NCP−CNS composites; CV curves of NCP−CNS-2 on graphite paper, BET surface areas, and pore size distributions of ZIF-8 with different particle sizes and their derived NCPs; electrical conductivity parameters of the NCP−CNS composites; and BET surface areas and pore size distributions of the NCP−CNS-2 prepared at different heating rates (PDF)

■ AUTHOR INFORMATION

Corresponding Authors
*E-mail: czhang@dhu.edu.cn (C.Z.).
*E-mail: txliu@dhu.edu.cn, txliu@fudan.edu.cn (T.L.).

ORCID Ⓘ
Jixin Zhu: 0000-0001-8749-8937
Jingsan Xu: 0000-0003-1172-3864
Chao Zhang: 0000-0003-1255-7183
Tianxi Liu: 0000-0002-5592-7386

Research Article

■ REFERENCES

(1) Simon, P.; Gogotsi, Y.; Dunn, B. Where Do Batteries End and Supercapacitors Begin? *Science* **2014**, *343*, 1210−1211.

(2) Liu, Z.; Jiang, L.; Sheng, L.; Zhou, Q.; Wei, T.; Zhang, B.; Fan, Z. Oxygen Clusters Distributed in Graphene with "Paddy Land" Structure: Ultrahigh Capacitance and Rate Performance for Supercapacitors. *Adv. Funct. Mater.* **2018**, *28*, 1705258.

(3) Sheng, L.; Jiang, L.; Wei, T.; Liu, Z.; Fan, Z. Spatial Charge Storage within Honeycomb-Carbon Frameworks for Ultrafast Supercapacitors with High Energy and Power Densities. *Adv. Energy Mater.* **2017**, *7*, 1700668.

(4) Hong, X.; Zhang, B.; Murphy, E.; Zou, J.; Kim, F. Three-Dimensional Reduced Graphene Oxide/Polyaniline Nanocomposite Film Prepared by Diffusion Driven Layer-By-Layer Assembly for High-Performance Supercapacitors. *J. Power Sources* **2017**, *343*, 60−66.

(5) Suleman, M.; Othman, M. A. R.; Hashmi, S. A.; Kumar, Y.; Deraman, M.; Omar, R.; Jasni, M. R. M. Activated Graphene Oxide/Reduced Graphene Oxide Electrodes and Low Viscous Sulfonium Cation Based Ionic Liquid Incorporated Flexible Gel Polymer Electrolyte for High Rate Supercapacitors. *J. Alloys Compd.* **2017**, *695*, 3376−3392.

(6) Wang, C.-C.; Liang, J.; Liao, Y.-H.; Lu, S.-Y. 3D Porous Graphene Nanostructure from a Simple, Fast, Scalable Process for High Performance Flexible Gel-Type Supercapacitors. *ACS Sustainable Chem. Eng.* **2017**, *5*, 4457−4467.

(7) He, D.; Niu, J.; Dou, M.; Ji, J.; Huang, Y.; Wang, F. Nitrogen and Oxygen Co-Doped Carbon Networks with a Mesopore-Dominant Hierarchical Porosity for High Energy and Power Density Supercapacitors. *Electrochim. Acta* **2017**, *238*, 310−318.

(8) Htut, K. Z.; Kim, M.; Lee, E.; Lee, G.; Baeck, S. H.; Shim, S. E. Biodegradable Polymer-Modified Graphene/Polyaniline Electrodes for Supercapacitors. *Synth. Met.* **2017**, *227*, 61−70.

(9) Lee, M. S.; Choi, H.-J.; Baek, J.-B.; Chang, D. W. Simple Solution-Based Synthesis of Pyridinic-Rich Nitrogen-Doped Graphene Nanoplatelets for Supercapacitors. *Appl. Energy* **2017**, *195*, 1071−1078.

(10) Suriani, A. B.; Nurhafizah, M. D.; Mohamed, A.; Masrom, A. K.; Mamat, M. H.; Malek, M. F.; Ahmad, M. K.; Rosmi, M. S.; Tanemura, M. Electrical Enhancement of Radiation-Vulcanized Natural Rubber Latex Added with Reduced Graphene Oxide Additives for Supercapacitor Electrodes. *J. Mater. Sci.* **2017**, *52*, 6611−6622.

(11) Niu, J.; Shao, R.; Liu, M.; Liang, J.; Zhang, Z.; Dou, M.; Huang, Y.; Wang, F. Porous Carbon Electrodes with Battery-Capacitive Storage Features for High Performance Li-Ion Capacitors. *Energy Storage Mater.* **2018**, *12*, 145−152.

(12) Chen, J. S.; Guan, C.; Gui, Y.; Blackwood, D. J. Rational Design of Self-Supported Ni3S2 Nanosheets Array for Advanced Asymmetric Supercapacitor with a Superior Energy Density. *ACS Appl. Mater. Interfaces* **2017**, *9*, 496−504.

(13) Niu, J.; Shao, R.; Liang, J.; Dou, M.; Li, Z.; Huang, Y.; Wang, F. Biomass-Derived Mesopore-Dominant Porous Carbons with Large Specific Surface Area and High Defect Density as High Performance Electrode Materials for Li-Ion Batteries and Supercapacitors. *Nano Energy* **2017**, *36*, 322−330.

(14) Sun, C.; Yang, J.; Rui, X.; Zhang, W.; Yan, Q.; Chen, P.; Huo, F.; Huang, W.; Dong, X. MOF-Directed Templating Synthesis of a

Porous Multicomponent Dodecahedron with Hollow Interiors for Enhanced Lithium-Ion Battery Anodes. *J. Mater. Chem. A* **2015**, *3*, 8483−8488.

(15) Lu, G.; Cui, C.; Zhang, W.; Liu, Y.; Huo, F. Synthesis and Self-Assembly of Monodispersed Metal-Organic Framework Microcrystals. *Chem.−Asian J.* **2013**, *8*, 69−72.

(16) Zhang, W.; Lu, G.; Li, S.; Liu, Y.; Xu, H.; Cui, C.; Yan, W.; Yang, Y.; Huo, F. Controlled Incorporation of Nanoparticles in Metal-Organic Framework Hybrid Thin Films. *Chem. Commun.* **2014**, *50*, 4296−4298.

(17) Li, S.; Shi, W.; Lu, G.; Li, S.; Loo, S. C. J.; Huo, F. Unconventional Nucleation and Oriented Growth of ZIF-8 Crystals on Non-Polar Surface. *Adv. Mater.* **2012**, *24*, 5954−5958.

(18) Li, S.; Zhang, W.; Huo, F. The Structural and Catalytic Properties of Nanoparticles@MOF Composites: A Case Study of Au@ZIF-8 Hybrid Crystals. *Phys. E* **2015**, *69*, 56−60.

(19) Banerjee, R.; Phan, A.; Wang, B.; Knobler, C.; Furukawa, H.; O'Keeffe, M.; Yaghi, O. M. High-Throughput Synthesis of Zeolitic Imidazolate Frameworks and Application to CO2 Capture. *Science* **2008**, *319*, 939−943.

(20) Park, K. S.; Ni, Z.; Cote, A. P.; Choi, J. Y.; Huang, R.; Uribe-Romo, F. J.; Chae, H. K.; O'Keeffe, M.; Yaghi, O. M. Exceptional Chemical and Thermal Stability of Zeolitic Imidazolate Frameworks. *Proc. Natl. Acad. Sci. U.S.A.* **2006**, *103*, 10186−10191.

(21) Phan, A.; Doonan, C. J.; Uribe-Romo, F. J.; Knobler, C. B.; O'Keeffe, M.; Yaghi, O. M. Synthesis, Structure, and Carbon Dioxide Capture Properties of Zeolitic Imidazolate Frameworks. *Acc. Chem. Res.* **2010**, *43*, 58−67.

(22) Zhao, X.; Yang, H.; Jing, P.; Shi, W.; Yang, G.; Cheng, P. A Metal-Organic Framework Approach toward Highly Nitrogen-Doped Graphitic Carbon as a Metal-Free Photocatalyst for Hydrogen Evolution. *Small* **2017**, *13*, 1603279.

(23) Gao, F.; Qu, J.; Geng, C.; Shao, G.; Wu, M. Self-Templating Synthesis of Nitrogen-Decorated Hierarchical Porous Carbon from Shrimp Shell for Supercapacitors. *J. Mater. Chem. A* **2016**, *4*, 7445−7452.

(24) He, X.; Ma, H.; Wang, J.; Xie, Y.; Xiao, N.; Qiu, J. Porous Carbon Nanosheets from Coal Tar for High-Performance Supercapacitors. *J. Power Sources* **2017**, *357*, 41−46.

(25) He, X.; Liu, Z.; Ma, H.; Zhang, N.; Yu, M.; Wu, M. Shell-Like Hierarchical Porous Carbons for High-Rate Performance Supercapacitors. *Microporous Mesoporous Mater.* **2016**, *236*, 134−140.

(26) He, X.; Zhang, N.; Shao, X.; Wu, M.; Yu, M.; Qiu, J. A Layered-Template-Nanospace-Confinement Strategy for Production of Corrugated Graphene Nanosheets from Petroleum Pitch for Supercapacitors. *Chem. Eng. J.* **2016**, *297*, 121−127.

(27) Qu, J.; Geng, C.; Lv, S.; Shao, G.; Ma, S.; Wu, M. Nitrogen, Oxygen and Phosphorus Decorated Porous Carbons Derived from Shrimp Shells for Supercapacitors. *Electrochim. Acta* **2015**, *176*, 982−988.

(28) Gao, F.; Shao, G.; Qu, J.; Lv, S.; Li, Y.; Wu, M. Tailoring of Porous and Nitrogen-Rich Carbons Derived from Hydrochar for High-Performance Supercapacitor Electrodes. *Electrochim. Acta* **2015**, *155*, 201−208.

(29) Banerjee, R.; Furukawa, H.; Britt, D.; Knobler, C.; O'Keeffe, M.; Yaghi, O. M. Control of Pore Size and Functionality in Isoreticular Zeolitic Imidazolate Frameworks and their Carbon Dioxide Selective Capture Properties. *J. Am. Chem. Soc.* **2009**, *131*, 3875−3877.

(30) Chmiola, J.; Yushin, G.; Gogotsi, Y.; Portet, C.; Simon, P.; Taberna, P. L. Anomalous Increase in Carbon Capacitance at Pore Sizes Less Than 1 Nanometer. *Science* **2006**, *313*, 1760−1763.

(31) Shao, R.; Niu, J.; Liang, J.; Liu, M.; Zhang, Z.; Dou, M.; Huang, Y.; Wang, F. Mesopore- and Macropore-Dominant Nitrogen-Doped Hierarchically Porous Carbons for High-Energy and Ultrafast Supercapacitors in Non-Aqueous Electrolytes. *ACS Appl. Mater. Interfaces* **2017**, *9*, 42797−42805.

(32) Zhang, Y.; Liu, S.; Zheng, X.; Wang, X.; Xu, Y.; Tang, H.; Kang, F.; Yang, Q.-H.; Luo, J. Biomass Organs Control the Porosity of Their Pyrolyzed Carbon. *Adv. Funct. Mater.* **2017**, *27*, 1604687.

(33) Qie, L.; Chen, W.; Xu, H.; Xiong, X.; Jiang, Y.; Zou, F.; Hu, X.; Xin, Y.; Zhang, Z.; Huang, Y. Synthesis of Functionalized 3D Hierarchical Porous Carbon for High-Performance Supercapacitors. *Energy Environ. Sci.* **2013**, *6*, 2497−2504.

(34) Wang, D.-W.; Li, F.; Liu, M.; Lu, G. Q.; Cheng, H.-M. 3D Aperiodic Hierarchical Porous Graphitic Carbon Material for High-Rate Electrochemical Capacitive Energy Storage. *Angew. Chem., Int. Ed.* **2008**, *47*, 373−376.

(35) Torad, N. L.; Hu, M.; Kamachi, Y.; Takai, K.; Imura, M.; Naito, M.; Yamauchi, Y. Facile Synthesis of Nanoporous Carbons with Controlled Particle Sizes by Direct Carbonization of Monodispersed ZIF-8 Crystals. *Chem. Commun.* **2013**, *49*, 2521−2523.

(36) Rafti, M.; Marmisollé, W. A.; Azzaroni, O. Metal-Organic Frameworks Help Conducting Polymers Optimize the Efficiency of the Oxygen Reduction Reaction in Neutral Solutions. *Adv. Mater. Interfaces* **2016**, *3*, 1600047.

(37) Schejn, A.; Balan, L.; Falk, V.; Aranda, L.; Medjahdi, G.; Schneider, R. Controlling ZIF-8 Nano- and Microcrystal Formation and Reactivity Through Zinc Salt Variations. *CrystEngComm* **2014**, *16*, 4493−4500.

(38) Choi, S.; Lee, H. J.; Oh, M. Facile Synthesis of Au or Ag Nanoparticles-Embedded Hollow Carbon Microspheres from Metal-Organic Framework Hybrids and Their Efficient Catalytic Activities. *Small* **2016**, *12*, 2425−2431.

(39) Kumar, R.; Jayaramulu, K.; Maji, T. K.; Rao, C. N. R. Hybrid Nanocomposites of ZIF-8 with Graphene Oxide Exhibiting Tunable Morphology, Significant CO2 Uptake and Other Novel Properties. *Chem. Commun.* **2013**, *49*, 4947−4949.

(40) Yan, J.; Wang, Q.; Wei, T.; Jiang, L.; Zhang, M.; Jing, X.; Fan, Z. Template-Assisted Low Temperature Synthesis of Functionalized Graphene for Ultrahigh Volumetric Performance Supercapacitors. *ACS Nano* **2014**, *8*, 4720−4729.

(41) Wan, L.; Wei, J.; Liang, Y.; Hu, Y.; Chen, X.; Shamsaei, E.; Ou, R.; Zhang, X.; Wang, H. ZIF-Derived Nitrogen-Doped Carbon/3D Graphene Frameworks for All-Solid-State Supercapacitors. *RSC Adv.* **2016**, *6*, 76575−76581.

(42) Yang, Z. K.; Lin, L.; Xu, A.-W. 2D Nanoporous Fe-N/C Nanosheets as Highly Efficient Non-Platinum Electrocatalysts for Oxygen Reduction Reaction in Zn-Air Battery. *Small* **2016**, *12*, 5710−5719.

(43) Kuang, Q.; Xie, S.-Y.; Jiang, Z.-Y.; Zhang, X.-H.; Xie, Z.-X.; Huang, R.-B.; Zheng, L.-S. Low Temperature Solvothermal Synthesis of Crumpled Carbon Nanosheets. *Carbon* **2004**, *42*, 1737−1741.

(44) Viculis, L. M.; Mack, J. J.; Mayer, O. M.; Hahn, H. T.; Kaner, R. B. Intercalation and Exfoliation Routes to Graphite Nanoplatelets. *J. Mater. Chem.* **2005**, *15*, 974−978.

(45) Sugimoto, W.; Iwata, H.; Yasunaga, Y.; Murakami, Y.; Takasu, Y. Preparation of Ruthenic Acid Nanosheets and Utilization of Its Interlayer Surface for Electrochemical Energy Storage. *Angew. Chem., Int. Ed.* **2003**, *42*, 4092−4096.

(46) Jiang, Y.; Yan, J.; Wu, X.; Shan, D.; Zhou, Q.; Jiang, L.; Yang, D.; Fan, Z. Facile Synthesis of Carbon Nanofibers-Bridged Porous Carbon Nanosheets for High-Performance Supercapacitors. *J. Power Sources* **2016**, *307*, 190−198.

(47) Dresselhaus, M. S.; Jorio, A.; Hofmann, M.; Dresselhaus, G.; Saito, R. Perspectives on Carbon Nanotubes and Graphene Raman Spectroscopy. *Nano Lett.* **2010**, *10*, 751−758.

(48) Ni, Z. H.; Yu, T.; Lu, Y. H.; Wang, Y. Y.; Feng, Y. P.; Shen, Z. X. Uniaxial Strain on Graphene: Raman Spectroscopy Study and Band-Gap Opening. *ACS Nano* **2008**, *2*, 2301−2305.

(49) Ghamsari, B. G.; Olivieri, A.; Variola, F.; Berini, P. Frequency Pulling and Line-Shape Broadening in Graphene Raman Spectra by Resonant Stokes Surface Plasmon Polaritons. *Phys. Rev. B: Condens. Matter Mater. Phys.* **2015**, *91*, 201408.

(50) Munn, A. S.; Dunne, P. W.; Tang, S. V. Y.; Lester, E. H. Large-Scale Continuous Hydrothermal Production and Activation of ZIF-8. *Chem. Commun.* **2015**, *51*, 12811−12814.

(51) Niu, J.; Liang, J.; Shao, R.; Liu, M.; Dou, M.; Li, Z.; Huang, Y.; Wang, F. Tremella-Like N,O-Codoped Hierarchically Porous Carbon Nanosheets as High-Performance Anode Materials for High Energy and Ultrafast Na-Ion Capacitors. *Nano Energy* **2017**, *41*, 285−292.

(52) Young, C.; Salunkhe, R. R.; Tang, J.; Hu, C.-C.; Shahabuddin, M.; Yanmaz, E.; Hossain, M. S. A.; Kim, J. H.; Yamauchi, Y. Zeolitic Imidazolate Framework (ZIF-8) Derived Nanoporous Carbon: The Effect of Carbonization Temperature on the Supercapacitor Performance in an Aqueous Electrolyte. *Phys. Chem. Chem. Phys.* **2016**, *18*, 29308−29315.

(53) Salunkhe, R. R.; Kamachi, Y.; Torad, N. L.; Hwang, S. M.; Sun, Z.; Dou, S. X.; Kim, J. H.; Yamauchi, Y. Fabrication of Symmetric Supercapacitors Based on MOF-Derived Nanoporous Carbons. *J. Mater. Chem. A* **2014**, *2*, 19848−19854.

(54) Gao, Y.; Wu, J.; Zhang, W.; Tan, Y.; Zhao, J.; Tang, B. The Electrochemical Performance of SnO2 Quantum Dots@Zeolitic Imidazolate Frameworks-8 (ZIF-8) Composite Material for Supercapacitors. *Mater. Lett.* **2014**, *128*, 208−211.

(55) Tang, J.; Salunkhe, R. R.; Liu, J.; Torad, N. L.; Imura, M.; Furukawa, S.; Yamauchi, Y. Thermal Conversion of Core-Shell Metal-Organic Frameworks: A New Method for Selectively Functionalized Nanoporous Hybrid Carbon. *J. Am. Chem. Soc.* **2015**, *137*, 1572−1580.

(56) Jiang, X.; Sun, L. X.; Xu, F. ZIF-8 Derived Graphene-Based Nitrogen-Doped Porous Carbonas Highly Efficient Supercapacitor Electrodes. *Mater. Sci. Forum* **2016**, *852*, 829−834.

(57) Wan, K.; Liu, S.; Zhang, C.; Li, L.; Zhao, Z.; Liu, T.; Xie, Y. Supramolecular Assembly of 1D Pristine Carbon Nanotubes and 2D Graphene Oxides into Macroscopic All-Carbon Hybrid Sponges for High-Energy-Density Supercapacitors. *ChemNanoMat* **2017**, *3*, 447−453.

(58) He, X.; Li, X.; Ma, H.; Han, J.; Zhang, H.; Yu, C.; Xiao, N.; Qiu, J. ZnO Template Strategy for the Synthesis of 3D Interconnected Graphene Nanocapsules from Coal Tar Pitch as Supercapacitor Electrode Materials. *J. Power Sources* **2017**, *340*, 183−191.

(59) Xie, X.; He, X.; Shao, X.; Dong, S.; Xiao, N.; Qiu, J. Synthesis of Layered Microporous Carbons from Coal Tar by Directing, Space-Confinement and Self-Sacrificed Template Strategy for Supercapacitors. *Electrochim. Acta* **2017**, *246*, 634−642.

(60) Young, C.; Salunkhe, R. R.; Alshehri, S. M.; Ahamad, T.; Huang, Z.; Henzie, J.; Yamauchi, Y. High Energy Density Supercapacitors Composed of Nickel Cobalt Oxide Nanosheets on Nanoporous Carbon Nanoarchitectures. *J. Mater. Chem. A* **2017**, *5*, 11834−11839.

(61) Liu, Y.; Li, G.; Chen, Z.; Peng, X. CNT-Threaded N-doped Porous Carbon Film as Binder-Free Electrode for High-Capacity Supercapacitor and Li−S Battery. *J. Mater. Chem. A* **2017**, *5*, 9775−9784.

(62) Li, X.; Hao, C.; Tang, B.; Wang, Y.; Liu, M.; Wang, Y.; Zhu, Y.; Lu, C.; Tang, Z. Supercapacitor Electrode Materials with Hierarchically Structured Pores from Carbonization of MWCNTs and ZIF-8 Composites. *Nanoscale* **2017**, *9*, 2178−2187.

(63) Wan, L.; Shamsaei, E.; Easton, C. D.; Yu, D.; Liang, Y.; Chen, X.; Abbasi, Z.; Akbari, A.; Zhang, X.; Wang, H. ZIF-8 Derived Nitrogen-Doped Porous Carbon/Carbon Nanotube Composite for High-Performance Supercapacitor. *Carbon* **2017**, *121*, 330−336.

(64) Jiang, M.; Cao, X.; Zhu, D.; Duan, Y.; Zhang, J. Hierarchically Porous N-doped Carbon Derived from ZIF-8 Nanocomposites for Electrochemical Applications. *Electrochim. Acta* **2016**, *196*, 699−707.

(65) Salunkhe, R. R.; Young, C.; Tang, J.; Takei, T.; Ide, Y.; Kobayashi, N.; Yamauchi, Y. A High-Performance Supercapacitor Cell Based on ZIF-8-Derived Nanoporous Carbon Using an Organic Electrolyte. *Chem. Commun.* **2016**, *52*, 4764−4767.

(66) Zhang, Y.; Lin, B.; Wang, J.; Tian, J.; Sun, Y.; Zhang, X.; Yang, H. All-Solid-State Asymmetric Supercapacitors Based on ZnO Quantum Dots/Carbon/CNT and Porous N-Doped Carbon/CNT Electrodes Derived from a Single ZIF-8/CNT Template. *J. Mater. Chem. A* **2016**, *4*, 10282−10293.

(67) Zhong, S.; Zhan, C.; Cao, D. Zeolitic Imidazolate Framework-Derived Nitrogen-Doped Porous Carbons as High Performance Supercapacitor Electrode Materials. *Carbon* **2015**, *85*, 51−59.

(68) Weng, Q.; Wang, X.; Wang, X.; Zhang, C.; Jiang, X.; Bando, Y.; Golberg, D. Supercapacitive Energy Storage Performance of

Molybdenum Disulfide Nanosheets Wrapped with Microporous Carbons. *J. Mater. Chem. A* **2015**, *3*, 3097−3102.

(69) Gao, Y.; Wu, J.; Zhang, W.; Tan, Y.; Gao, J.; Zhao, J.; Tang, B. The Calcined Zeolitic Imidazolate Framework-8 (ZIF-8) under Different Conditions as Electrode for Supercapacitor Applications. *J. Solid State Electrochem.* **2014**, *18*, 3203−3207.

(70) Yu, G.; Zou, X.; Wang, A.; Sun, J.; Zhu, G. Generation of Bimodal Porosity via Self-Extra Porogenes in Nanoporous Carbons for Supercapacitor Application. *J. Mater. Chem. A* **2014**, *2*, 15420−15427.

(71) Chaikittisilp, W.; Hu, M.; Wang, H.; Huang, H.-S.; Fujita, T.; Wu, K. C.-W.; Chen, L.-C.; Yamauchi, Y.; Ariga, K. Nanoporous Carbons through Direct Carbonization of a Zeolitic Imidazolate Framework for Supercapacitor Electrodes. *Chem. Commun.* **2012**, *48*, 7259−7261.

(72) Amali, A. J.; Sun, J.-K.; Xu, Q. From Assembled Metal-Organic Framework Nanoparticles to Hierarchically Porous Carbon for Electrochemical Energy Storage. *Chem. Commun.* **2014**, *50*, 1519−1522.